

# DetVPCC: RoI-based Point Cloud Sequence Compression for 3D Object Detection

Mingxuan Yan\* Ruijie Zhang\* Xuedou Xiao Wei Wang<sup>†</sup>  
Huazhong University of Science and Technology

## Abstract

While MPEG-standardized video-based point cloud compression (VPCC) achieves high compression efficiency for human perception, it struggles with a poor trade-off between bitrate savings and detection accuracy when supporting 3D object detectors. This limitation stems from VPCC’s inability to prioritize regions of different importance within point clouds. To address this issue, we propose DetVPCC, a novel method integrating region-of-interest (RoI) encoding with VPCC for efficient point cloud sequence compression while preserving the 3D object detection accuracy. Specifically, we augment VPCC to support RoI-based compression by assigning spatially non-uniform quality levels. Then, we introduce a lightweight RoI detector to identify crucial regions that potentially contain objects. Experiments on the nuScenes dataset demonstrate that our approach significantly improves the detection accuracy. The code and demo video are available in supplementary materials.

## 1. Introduction

Point cloud-based 3D object detection is revolutionizing a wide range of applications, significantly enhancing capabilities in fields such as autonomous driving [13, 30, 52] and 3D scene perception [5, 6, 18, 47]. Due to the conflict between computationally intensive deep learning-based 3D object detectors and the limited computational resources of edge devices, it is promising to stream or archive point clouds to compute-capable platforms for further analytics [26, 31] or model optimization [40, 50]. However, the large volumes of point cloud data generated by sensors pose significant challenges for networking and storage.

The moving picture experts group’s (MPEG) video-based point cloud compression (VPCC) [17] standard is a promising solution to point cloud sequence compression.

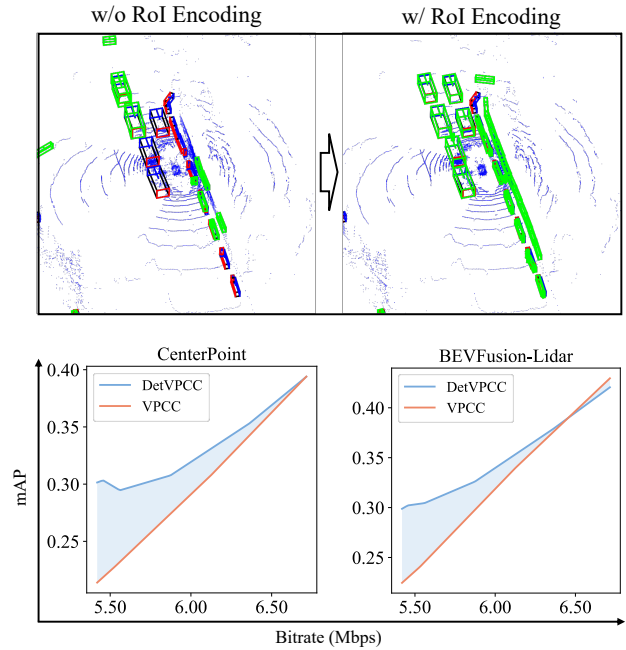


Figure 1. The first row demonstrates the accuracy improvement of 3D object detection after applying RoI encoding (objects detected are colored in green). The second row shows the accuracy-bitrate trade-off curve of DetVPCC and VPCC when supporting CenterPoint [51] and BEVFusion-Lidar [29].<sup>1</sup>

VPCC projects a sequence of 3D point clouds into 2D depth and color images, and leverages mature video codecs such as H.264 [46], which is widely supported by existing hardware, to remove temporal redundancy and compress the volume [16]. Typically, VPCC does not prioritize different spatial regions and applies a constant compression quality within a point cloud, which is aligned with visual quality metrics such as Point-to-Point (P2P) PSNR [32] and Point-to-Plane (P2C) PSNR [43].

However, this quality assignment scheme poses significant limitations in applications where some spatial regions, i.e., regions of interest (RoIs), demand higher fidelity. For instance, in driving scenes, regions containing the potential objects are crucial for 3D object detectors [35, 36], while the ground plane is less interested [19, 24]. The uniform

\*Equal contribution

<sup>†</sup>Corresponding Author

<sup>1</sup>Results in the first row are encoded with nuScenes [7] dataset, RoI QP  $q_r = 20$ , background QP  $q_b = 45$ , CenterPoint [51] as the back-end 3D object detector. Settings of results in the second row follow Fig. 5. Details about RoI encoding can be found in Sec. 3.2.

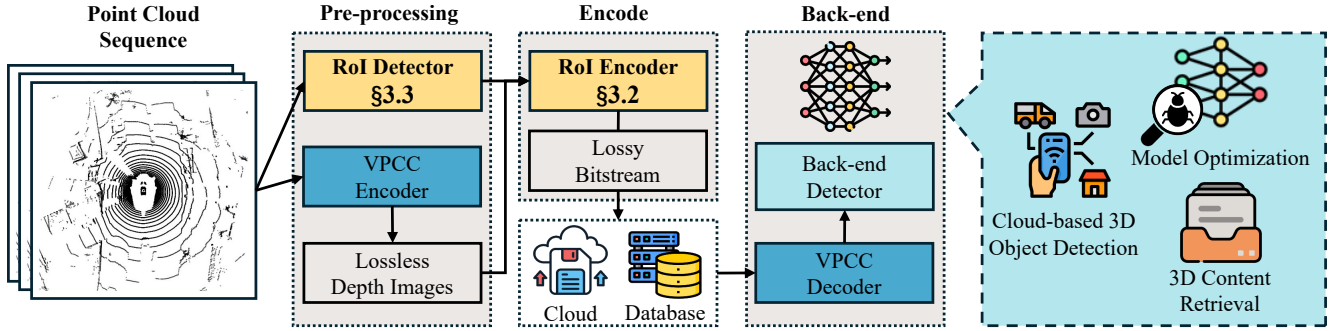


Figure 2. Overview of DetVPCC.

application of compression may result in the loss of critical details in RoIs, potentially compromising the functionality of 3D object detectors. To better understand this dilemma, Fig. 1 demonstrates the bitrate-accuracy curve of VPCC when applying VPCC on nuScenes dataset [7]. As shown, VPCC experiences a poor trade-off between bitrate reduction and 3D object detection accuracy.

To this end, we propose DetVPCC, a RoI-based point cloud sequence compression method. Specifically, we enhance VPCC to support RoI encoding and design a lightweight detector to locate RoIs efficiently. As shown in Fig. 1, with the aid of RoI encoding, our method significantly improves the accuracy of 3D object detectors.

The contributions of this work are as follows:

- To our knowledge, this is the first study that highlights and addresses the poor bitrate-accuracy trade-off of VPCC when it supports 3D object detection.
- We enhance VPCC to support RoI-based encoding to allow spatially non-uniform quality assignment.
- We design an efficient RoI detector to locate critical regions potentially containing objects.
- We evaluate DetVPCC on the nuScenes dataset. Experimental results show that DetVPCC achieves a better bitrate-accuracy trade-off than vanilla VPCC.

## 2. Related Work

### 2.1. Point Cloud Sequence Compression

Point cloud sequence compression methods can be broadly categorized into point-based and projection-based methods. Point-based methods directly operate on 3D point clouds to remove redundant content across frames. While early methods represent points as octree [14] or voxels [9], recent approaches [2, 15] leverage deep neural networks (DNNs) to transform unstructured point clouds into latent spaces, improving coding efficiency by better correlating similar components between frames. In contrast, projection-based methods project the 3D point cloud to 2D depth images and compress the volume of depth images [16, 42]. As part of ongoing standardization efforts, VPCC [16] utilizes mature

2D video encoders like H.264 to encode depth and color images. This strategy makes VPCC one of the most promising point cloud sequence compression standards due to its seamless integration with existing 2D video encoders and hardware infrastructure.

### 2.2. Encoders for Machine Vision

As vision models consume increasing multimedia content, there is growing interest in developing machine vision-oriented encoders that aim to save bits by exploiting RoIs of vision models. For 2D video encoding, feedback-based methods [10, 25, 28, 48, 49] exploits either gradient-based importance scores or predicted bounding boxes to build spatial importance maps. Neural encoder-based methods [37, 45] replace traditional encoders with differential neural encoders and directly optimize them to support the target vision model. On-device analytics methods [11, 33, 53] propose to use cheap analytics models to localize RoIs or dynamically control encoding parameters. For single-frame 3D point cloud encoding, Liu et al. [27] propose a neural encoder optimized for both human and machine perception. However, to our knowledge, none of the existing works have yet investigated 3D point cloud sequence compression.

## 3. Methodology

### 3.1. Overview

As shown in Fig. 2, in the first stage, the RoI detector identifies RoIs within point clouds, while VPCC converts raw point clouds into lossless 2D depth images. Subsequently, the RoI encoder applies RoI-based lossy transcoding to these lossless depth images, effectively compressing the data volume. The encoded point clouds can then be archived or streamed to the cloud for further analysis by back-end 3D object detectors. This enables various applications, such as cloud-based 3D object detection, fault detection, optimization of on-device 3D object detectors, and efficient 3D content retrieval.

## 3.2. RoI-based point cloud Sequence Encoder

### 3.2.1 Preliminary on VPCC

To encode a point cloud sequence, VPCC first clusters point clouds into small patches grouped by point-wise surface normals. Then, it projects and arranges them into three sequences of 2D images, namely attribute, occupancy, and geometry images [16]. Attribute images store color and auxiliary information. Occupancy images are binary images indicating the occupancies in geometry images. Geometry (Depth) images encode point positions into pixel values proportional to the distance between the projection plane and correlated points, as shown in Fig. 3. These 2D images are then compressed to separate bitstreams using standard 2D video codecs like H.264. Typically, geometry images account for most of the volume [39].

To reconstruct point clouds, the compressed bitstreams are decoded and projected back to 3D point clouds using projection information encoded in the bitstream.

### 3.2.2 Bitrate Control and RoI Encoding

VPCC provides bitrate control options at both point and image levels. For the point-level bitrate control, VPCC provides options to limit the maximum number of points in a patch and the maximum distance between a selected point to the projection plane [16]. At the image level, bitrate control follows the underlying 2D video encoder.

Following the practice of existing works [39, 41, 44], we control bitrate at the image level by *transcoding the lossless geometry (depth) images* with H.264 [46] video encoder to take advantage of the mature bitrate control mechanisms of 2D video encoders. Unlike previous works that uniformly compress geometry images, we implement non-uniform quality assignments by leveraging the macroblock-level quality control feature of 2D video encoders.

Specifically, H.264 processes geometry images in units of macroblocks consisting of  $16 \times 16$  pixels. Each macroblock will be further partitioned and transformed into the frequency domain by  $4 \times 4$  2D discrete cosine transform (DCT) [46]:

$$\mathbf{Y} = \mathbf{A}\mathbf{X}\mathbf{A}^T$$

where  $\mathbf{X}$  is the  $4 \times 4$  pixel matrix,  $\mathbf{Y}$  is the DCT coefficient matrix,  $\mathbf{A}$  is the orthogonal DCT transform matrix. The above equation could be transformed into the following equivalent form [38]:

$$\mathbf{Y} = (\mathbf{C}\mathbf{X}\mathbf{C}^T) \otimes \mathbf{E}$$

<sup>2</sup>For better visualization, the depth image is cropped, and its sharpness is lowered by 25%; The sample is encoded with  $q_r = 25$  and  $q_b = 30$ .

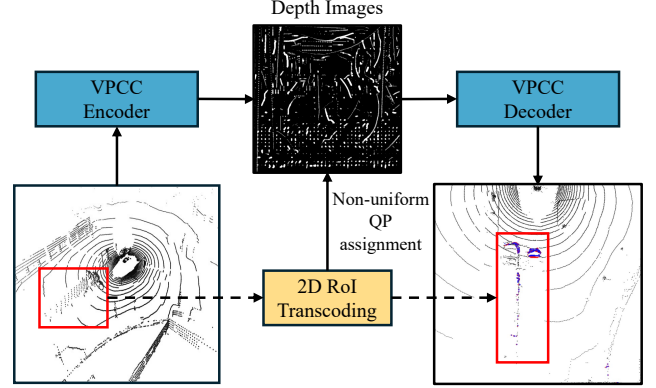


Figure 3. Illustration of RoI Encoding.<sup>2</sup> The right image compares point clouds with RoI and non-RoI encoding. The red points represent the points that appear in the non-RoI encoded frame but not in the RoI encoded frame, and blue represents the contrary. Black points represent common parts.

where  $\mathbf{E}$  is a scaling matrix, and  $\otimes$  represents element-wise multiplication.  $\mathbf{W} = \mathbf{C}\mathbf{X}\mathbf{C}^T$  is the unscaled coefficient matrix, which is quantized and scaled by:

$$\mathbf{Z}_{ij} = \text{round} \left( \mathbf{W}_{ij} \frac{\mathbf{M}_{ij}}{2^{(15 + \text{floor}(\frac{QP}{6}))}} \right) \quad (1)$$

where  $\mathbf{Z}$  is the quantized frequency coefficient matrix,  $\mathbf{M}$  is a scaling matrix derived from  $\mathbf{E}$ . QP, i.e., the quantization parameter, is an integral value that controls bitrate by adjusting the quantization step. *The larger the QP is, the less frequency information is reserved during the quantization, the lower the image quality, and the smaller the volume.* In H.264, QP ranges from 0 to 51.

To implement non-uniform QP assignments, we use the emphasis map feature provided by NVENCODE API [34]. This feature allows *macroblock-level control of QP*, which enables the encoder to enhance the quality of geometry images in specified partitions. As illustrated in Fig. 3, by setting a lower QP for RoIs of depth images, the quality of RoIs in the decoded point clouds is enhanced. In DetVPCC, we use a binary quality assignment strategy by applying two distinct QPs—a low QP for RoIs and a high QP for non-RoI (background) areas.

### 3.2.3 Encoding Objective

The objective of the RoI encoder can be formalized as:

$$\max_{\mathbf{R}} \sum_{q_b \in Q_b} \mathcal{F}(q_b, q_r, \mathbf{R}) \quad (2)$$

$\mathbf{R} \in \{0, 1\}^{B \times L}$  is the binary RoI macroblock indicator where  $B, L$  denote the number of macroblocks in each frame and total number of frames of the geometry image sequence to be encoded;  $\mathcal{F}$  denotes the 3D object detector's

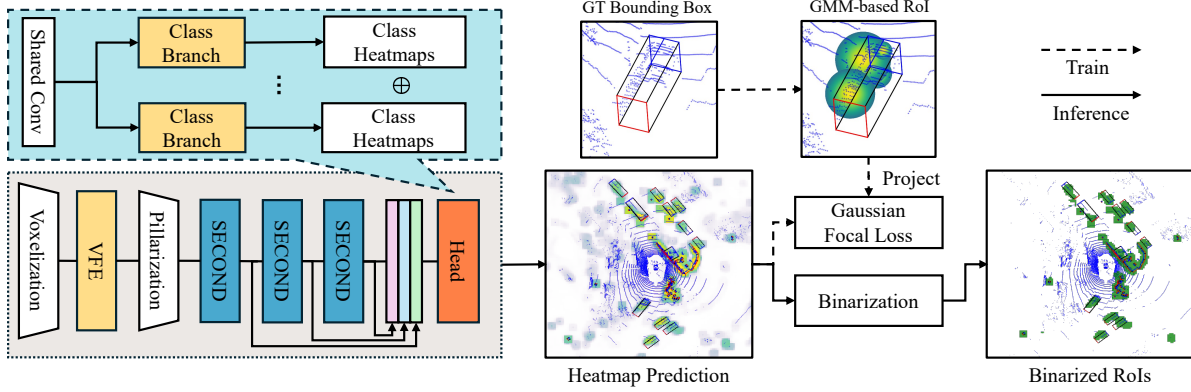


Figure 4. Design of the GMM-based ROI detector.

accuracy function;  $q_r$  is the pre-defined QP of ROI; the non-ROI (background) QP  $q_b$  is sampled from a pre-defined QP value set  $Q_b$  to comprehensively evaluate  $\mathbf{R}$  under different background point cloud qualities.

Typically, RoIs are detected in 3D space. A ROI mask of a given point cloud can be denoted by  $\mathcal{R} \in \{0, 1\}^N$  where  $N$  is the number of points in the point cloud and  $\mathcal{R}[n] = 1$  indicates the  $n^{\text{th}}$  point belongs to ROI. Typically,  $N > B$ .  $\mathbf{R}$  can be solved by:

$$\mathbf{M}^p_t \mathbf{M}^b_t \mathbf{R}[:, t] = \mathcal{R}_t^T \quad (3)$$

where  $M$  is the number of pixels in the frame;  $t$  is the frame index;  $\mathbf{M}^p \in \{0, 1\}^{N \times M}$  is the VPCC's point-to-pixel map encoded within the bitstream and  $\mathbf{M}^b \in \{0, 1\}^{M \times B}$  is the pixel-to-macroblock index map.

As such, the core of solving Eq. 2 is to identify the ROI mask  $\mathcal{R}$  for any given point cloud. In the next section, we will elaborate on the design of our ROI detector, which efficiently detects 3D RoIs.

### 3.3. ROI Detector

An intuitive design for the ROI detector is based on a lightweight 3D object detector, which uses the predicted 3D bounding box as the RoIs. However, while object detectors try to precisely regress the bounding box parameters, our goal is to gain point-level importance scores *without the need to distinguish between instances or predict the object classes*. This observation enables the ROI detector to be designed in a lightweight yet efficient way.

#### 3.3.1 GMM-based ROI

Inspired by previous heatmap-based object predictors [22, 51, 54, 55], the ROI detector is designed to predict a heatmap indicating the possibility an object appears in a given region.

As shown in Fig. 4, due to irregular object shapes and occlusion, points belonging to an object tend to be *distributed*

---

#### Algorithm 1 Find Points in Bounding Boxes

---

**Require:** Point cloud  $P = \{\mathbf{p}_i\}_{i=1}^N$ ; A set of bounding boxes  $\mathcal{B} = \{B_j\}_{j=1}^M$ , where  $B_j$  is defined by width  $w_j$ , length  $l_j$ , height  $h_j$  and box center  $\mathbf{c}_j$ .

**Ensure:** List of inner point clouds  $\mathcal{P}_{in} = \{P_j\}_{j=1}^M$

- 1:  $\mathcal{P}_{in} \leftarrow \emptyset$
  - 2:  $\mathcal{T} \leftarrow \text{BuildKDTree}(P)$
  - 3: **for** each bounding box  $B_j \in \mathcal{B}$  **do**
  - 4:    $r_j = \frac{1}{2} \sqrt{w_j^2 + l_j^2 + h_j^2}$
  - 5:    $P_r \leftarrow \mathcal{T}.\text{QueryBallPoints}(\mathbf{c}_j, r_j)$
  - 6:    $H_j \leftarrow \text{Delaunay}(\text{Corners}(B_j))$
  - 7:    $P_j \leftarrow H_j.\text{PointsInAnySimplex}(P_r)$
  - 8:    $\mathcal{P}_{in} \leftarrow \mathcal{P}_{in} \cup \{P_j\}$
  - 9: **end for**
  - 10: **return**  $\mathcal{P}_{in}$
- 

*in clusters*, and each cluster could be interpreted as a distinct component of that object. Thus, instead of using simple Gaussian distributions to model the object centers [51, 55], we propose to model the points of objects with 3D Gaussian mixture models (GMMs). Specifically, we assume the point cloud  $P = \{\mathbf{p}_i\}_{i=1}^N$  of an object is sampled from a 3D GMM:

$$\mathbf{p}_i \sim \sum_{c=1}^C \pi_c \mathcal{N}(\mathbf{p} \mid \boldsymbol{\mu}_c, \boldsymbol{\Sigma}_c) \quad (4)$$

where  $C$  is the number of Gaussian components in the mixture.  $\pi_c$  is the weight of the  $c$ -th Gaussian component, with  $\sum_{c=1}^C \pi_k = 1$  and  $\pi_c \geq 0$ . We let  $\pi_c = \frac{1}{C}, \forall c \in \{1, \dots, C\}$  as a general assumption for the priors. At training time, the component centers  $\boldsymbol{\mu}_c \in \mathbb{R}^3$  and covariances  $\boldsymbol{\Sigma}_c \in \mathbb{R}^{3 \times 3}$  is fitted to the points located inside of each ground-truth bounding box.

To accelerate the labeling process, we provide an efficient algorithm to find points inside a set of 3D bounding boxes in Alg. 1. The algorithm essentially leverages a

Table 1. Complexities of RoI detectors.

| Model    | GMM-based RoI |           | Naive RoI |           |
|----------|---------------|-----------|-----------|-----------|
|          | FLOPs (G)     | Param (M) | FLOPs (G) | Param (M) |
| Backbone | 28.51         | 4.21      | 37.50     | 4.26      |
| Header   | 20.49         | 0.51      | 28.22     | 1.72      |
| Total    | 49.00         | 4.72      | 65.72     | 5.98      |

reusable K-D tree to narrow the search space of each bounding box down to its circumscribed sphere. Then, we adopt Quickhull algorithm [4] to accelerate the searching process of finding points inside the sphere. Specifically, it performs Delaunay triangulation to separate the bounding box into a set of simplexes  $H$ , i.e., tetrahedrons in 3D space. Then, Alg. 1 iterate through  $P_r$  and check whether the point falls in any of the simplexes and get the points inside of the RoI bounding boxes  $\mathcal{P}_{in}$ .

To enable a lightweight network design of the RoI detector, we transform 3D GMMs to 2D heatmaps  $Y \in \mathbb{R}^{h \times w}$ . Specifically, we first project 3D GMMs on the x-y plane. Then, for heatmap grid  $(i, j)$ , its value is set to the maximum sampled probability across GMMs:

$$Y_{ij} = \max_k \sum_{c=1}^C \frac{1}{C} \mathcal{N}(\mu_{ij} | \mu'_{kc}, \Sigma'_{kc}) \quad (5)$$

where  $k \in \{1, \dots, K\}$ ,  $K$  is the total number of GMMs in the frame.  $\mu_{ij}$  is the center coordinate of the grid  $(i, j)$ ,  $\mu'$  and  $\Sigma'$  are parameters of projected 2D GMMs.

### 3.3.2 Network Design

As shown in Fig. 4, we borrowed the backbone of PointPillar [21] due to its lightweight design and efficiency. Following the design of CenterPoint [51], the head regresses on a pillar-wise RoI heatmap of  $C \times 200 \times 200$ , where  $C$  is the number of object classes. The regressed heatmap is supervised by Gaussian focal loss [22] separately on each class channel. At runtime, the heatmap  $Y$  produced by the network is binarized by a pre-defined threshold  $\gamma$  to rule out low-confident regions. Then, the heatmap takes union across class channels to aggregate class-wise RoIs. The aggregated binary heatmap  $Y_b \in \{0, 1\}^{200 \times 200}$  is then transformed to point-wise RoI mask  $\mathcal{R}_Y$ .

Table. 1 lists the FLOPs and number of parameters of the proposed network. *The overhead is below 50G FLOPs, and the number of parameters is less than 5M.*

To suppress ground points included in  $\mathcal{R}_Y$ , we utilize the ground removal algorithm Patchwork++ [23] to generate the foreground mask  $\mathcal{R}_f$ . Then, the final RoI mask is given by:

$$\mathcal{R} = \mathcal{R}_Y \cdot \mathcal{R}_f \quad (6)$$

## 4. Experiments

### 4.1. Experiment Settings

#### 4.1.1 Dataset

Experiments are conducted on the nuScenes [7] dataset, which comprises 1000 autonomous driving scenes, each lasting 20 seconds, collected in urban environments such as Boston and Singapore. Each scene sample includes data from a lidar sensor, which provides high-resolution 3D point clouds. The point clouds are sampled by a frequency of 20 Hz and annotated by a frequency of 2 Hz with 3D bounding boxes for 10 classes of objects.

For 3D object detection, nuScenes assigns 750 scenes for training, 150 scenes for validation, and 100 for testing. However, the annotations for the test set nuScenes dataset are not directly accessible [1]. As we need to conduct a vast number of rounds of evaluation on the test set, we re-split the training set to 525 for training and 125 for validation, and the original 150 scenes in the validation set are used for testing. The new splitting is applied to the training of both RoI detectors and back-end detectors.

As frames in the same scenes have close object distributions, we select clips of 40-point cloud frames indexing from 90 to 130 from each scene to accelerate the encoding process. Note that the input to the RoI detector is the enhanced point cloud that aggregates 10 historical lidar frames following common practices [8]. Thus, RoI detectors predict RoI mask  $\mathcal{R}$  on 4 out of the 40 frames. The RoI mask for the rest of the frames is transformed from  $\mathcal{R}$  based on the ego-motion provided by nuScenes.

#### 4.1.2 Back-end Detectors

We select the leading 3D object detectors, CenterPoint [51] and BEVFusion-Lidar [29] as our back-end detectors. We first pre-train the detectors using the dataset splitting in Sec. 4.1.1. To accommodate the back-end detectors with the compressed dataset, we fine-tune the pre-trained models on a mixed dataset comprising both lossy and lossless point clouds for one epoch. Details can be found in Suppl. 8.

#### 4.1.3 Baselines

We provide two baselines for the evaluation:

**Vanilla VPCC:** The original VPCC using a uniform compression scheme. The bitrate control is also implemented during the transcoding phase, except the whole point cloud is encoded with non-RoI QP  $q_b$ .

**Naive RoI:** Replace the GMM-based RoI detector of DetVPCC with a naive RoI detector directly built based on the CenterPoint [51] 3D object detector. The output 3D bounding boxes are transformed into point-level RoI indexes at the test time. The detector is trained on the same

Table 2. Comparison of RoI-based methods over vanilla VPCC. Outperforming results are highlighted in bold.

| Detector                       | CenterPoint |              |              |              |              |              | BEVFusion-Lidar |              |              |              |              |              |
|--------------------------------|-------------|--------------|--------------|--------------|--------------|--------------|-----------------|--------------|--------------|--------------|--------------|--------------|
|                                | Naive RoI   |              |              | DetVPCC      |              |              | Naive RoI       |              |              | DetVPCC      |              |              |
|                                | $q_r = 15$  | $q_r = 20$   | $q_r = 25$   | $q_r = 15$   | $q_r = 20$   | $q_r = 25$   | $q_r = 15$      | $q_r = 20$   | $q_r = 25$   | $q_r = 15$   | $q_r = 20$   | $q_r = 25$   |
| $\mathcal{A}_{mAP} \uparrow$   | -0.26       | 1.34         | 1.94         | <b>1.92</b>  | <b>3.51</b>  | <b>3.61</b>  | -1.61           | 0.21         | 1.24         | <b>0.29</b>  | <b>2.33</b>  | <b>2.80</b>  |
| $\mathcal{A}_{NDS} \uparrow$   | -1.00       | 1.20         | 2.26         | <b>1.34</b>  | <b>2.90</b>  | <b>3.69</b>  | -1.44           | -0.18        | 0.75         | <b>0.33</b>  | <b>1.65</b>  | <b>2.23</b>  |
| $\mathcal{A}_{ATE} \downarrow$ | -0.22       | -2.81        | -3.80        | <b>-1.75</b> | <b>-3.92</b> | <b>-4.40</b> | <b>0.49</b>     | -0.05        | -0.38        | 0.66         | <b>-0.07</b> | <b>-0.84</b> |
| $\mathcal{A}_{ASE} \downarrow$ | -0.72       | -1.92        | -2.82        | <b>-1.44</b> | <b>-2.50</b> | <b>-3.32</b> | <b>-0.02</b>    | <b>-0.37</b> | <b>-0.41</b> | 0.09         | 0.06         | -0.24        |
| $\mathcal{A}_{AOE} \downarrow$ | 4.56        | 1.64         | <b>-3.54</b> | <b>1.35</b>  | <b>-0.27</b> | -0.95        | 0.00            | -0.73        | 0.28         | <b>-2.14</b> | <b>-1.21</b> | <b>-0.26</b> |
| $\mathcal{A}_{AVE} \downarrow$ | 5.60        | 0.60         | 0.56         | <b>0.30</b>  | <b>-2.13</b> | <b>-5.89</b> | 5.63            | 4.11         | -0.25        | <b>-0.01</b> | <b>-2.73</b> | <b>-5.58</b> |
| $\mathcal{A}_{AAE} \downarrow$ | -0.56       | <b>-2.81</b> | -3.32        | <b>-2.27</b> | -2.65        | <b>-4.29</b> | 0.27            | -0.06        | -0.57        | <b>-0.44</b> | <b>-0.90</b> | <b>-1.34</b> |

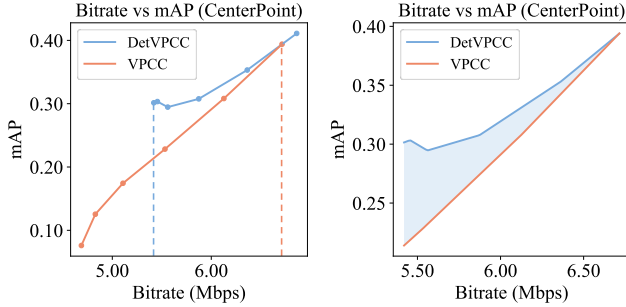


Figure 5. Illustration of the evaluation metric.<sup>4</sup>

dataset described in Sec. 4.1.1. Ground removal and RoI encoding follow the same procedure as DetVPCC.

To fairly compare the GMM-based RoI detector and naive RoI detector, the network capacity of the two detectors is comparable, as shown in Table. 1. The FLOPs and parameter number of the naive RoI detector are slightly larger than the GMM-based RoI detector.

#### 4.1.4 Implementation Details

We set the number of GMM components  $K = 5$  and the test-time heatmap binarization threshold  $\gamma = 0.4$ . We use MPEG-TMC2 test model v15.0<sup>3</sup> as the base implementation of VPCC. Details about the implementation and training of the RoI detector can be found in Suppl. 7.

#### 4.1.5 Metrics

For each  $q_r \in \{15, 20, 25\}$ , we iterate  $q_b \in \{30, 33, 36, 39, 42, 45\}$  to encode the test set. Then, we run back-end 3D object detectors on the encoded test set and record their performances. The performance metrics [7] include mean average precision (mAP), nuScenes detection score (NDS), and true-positive metrics: average translation error (ATE), average scale error (ASE), average orientation error (AOE), average velocity error (AVE) and average attribute error (AAE). We also record the averaged bitrate of

<sup>3</sup><https://github.com/MPEGGroup/mpeg-pcc-tmc2>

<sup>4</sup>Result is encoded with  $q_r = 25$ , the rest of the settings follows Sec. 4.1.4.

encoded bitstreams across test scenes. As shown in Fig. 5, we can draw metric-bitrate curves where the y-axis is the performance metric, and the x-axis is the averaged bitrates in megabits per second (Mbps).

We define *averaged advantage*  $\mathcal{A}$  to evaluate the performance boost brought by RoI encoding against vanilla VPCC:

$$\mathcal{A} = \frac{\int_{x_{min}}^{x_{max}} M(x) - M_b(x) dx}{x_{max} - x_{min}} \quad (7)$$

$$\approx \frac{1}{N} \sum_{i=1}^N M(x_i) - M_b(x_i)$$

where  $M$  and  $M_b$  are the metric-bitrate curves of the RoI-based method and vanilla VPCC, respectively.  $x_{min}$  and  $x_{max}$  define the region on the x-axis where the domains of the two curves overlap. We linearly interpolate the metric-volume line chart to approximate  $\mathcal{A}$ , where  $N = 100$  is the number of samples after interpolation. In the following experiments,  $\mathcal{A}$  is recorded in percentage value.

## 4.2. Main Results

Table. 2 shows the main results of the experiment. It can be seen that: 1) *DetVPCC consistently improves VPCC across different RoI QPs and back-end detectors.* 2) *The GMM-based RoI detector significantly outperforms naive RoI detector in most cases.* This shows that GMM-based RoI is more efficient for finding critical regions potentially containing objects. For the naive RoI detector, 3D object detection redundantly requires the network to classify the objects, which wastes the network’s capacity. 3) Compared with vanilla VPCC and naive RoI, *DetVPCC consistently improves the true-positive metrics.* This implies that with GMM-based RoI encoding, the details of objects are well-preserved so that the back-end detector can easily identify the boundary and pose of objects. 4) *The advantage over vanilla VPCC for both RoI-based methods enlarges when  $q_r$  increases.* This is partly because when the RoI quality is degraded, the domain of the metric-bitrate curves of RoI-based methods will shift towards low bitrates, where the advantage of RoI encoding is more significant. However,

Table 3. Class-wise performance of DetVPCC over vanilla VPCC. Results outperforming VPCC are highlighted in bold.

| Class                          | Car          | Truck        | Bus          | Trailer       | Constr Veh   | Pedestrian   | Motorcycle   | Bicycle       | Traffic Cone | Barrier      |
|--------------------------------|--------------|--------------|--------------|---------------|--------------|--------------|--------------|---------------|--------------|--------------|
| $\mathcal{A}_{mAP} \uparrow$   | -0.28        | <b>2.87</b>  | <b>2.53</b>  | <b>4.85</b>   | <b>1.13</b>  | <b>10.00</b> | <b>1.79</b>  | -0.50         | <b>1.05</b>  | <b>5.76</b>  |
| $\mathcal{A}_{ATE} \downarrow$ | <b>-0.09</b> | 0.81         | 0.25         | <b>-1.53</b>  | <b>-1.85</b> | <b>-0.57</b> | <b>-0.51</b> | <b>-13.19</b> | <b>-1.31</b> | <b>-1.97</b> |
| $\mathcal{A}_{ASE} \downarrow$ | <b>-0.13</b> | 0.07         | 0.40         | <b>-1.02</b>  | <b>-1.76</b> | 0.26         | <b>-0.06</b> | <b>-9.42</b>  | <b>-0.25</b> | <b>-0.30</b> |
| $\mathcal{A}_{AOE} \downarrow$ | <b>-0.66</b> | <b>-1.03</b> | <b>-0.25</b> | 7.39          | <b>-3.95</b> | <b>-2.39</b> | 2.96         | <b>-8.48</b>  | —            | <b>-0.25</b> |
| $\mathcal{A}_{AVE} \downarrow$ | <b>-0.84</b> | <b>-1.97</b> | <b>-3.94</b> | <b>-12.09</b> | 0.14         | <b>-1.32</b> | 2.47         | <b>-1.85</b>  | —            | —            |
| $\mathcal{A}_{AAE} \downarrow$ | <b>-0.43</b> | 0.04         | <b>-0.82</b> | <b>-1.06</b>  | 0.49         | <b>-2.41</b> | 1.82         | <b>-11.83</b> | —            | —            |

when  $q_r$  is too large, the absolute performance of the RoI-based methods will be less satisfying. Thus, we empirically keep  $q_r$  no larger than 25.

### 4.3. Additional Experiments

We conduct additional experiments to get a detailed understanding of DetVPCC’s performance. Unless specially mentioned, we set  $q_r = 20$ ,  $K = 5$ ,  $\gamma = 0.4$ , and  $\mathcal{A}$  is averaged across back-end detectors.

#### 4.3.1 Class-wise Analysis

Table 3 demonstrates the class-wise performance of DetVPCC over vanilla VPCC. It can be seen that: 1) *The smaller the object, the greater the performance improvement achieved by DetVPCC over VPCC.* For instance, the mAP advantage of *pedestrian* class improves significantly by 10%; the mAP advantages of *barrier* class improves by 5.76%; the ATE and AAE advantages of *bicycle* class improve over 10%. These results indicate that DetVPCC preserves much more object details than vanilla VPCC, given the same bitrate consumption. 2) *DetVPCC help distinguish between visually similar classes.* For instance, mAP advantages of *truck* and *bus* both improve by approximately 3%. 3) *Interestingly, the performances of car class are less significant compared to other classes.* It may be that the key features for identifying the *car* class are more resilient to VPCC compression.

#### 4.3.2 Number of GMM Components

Table 4. Impact of the number of GMM Components

| $K$                            | 1     | 3     | 5     | 7     |
|--------------------------------|-------|-------|-------|-------|
| $\mathcal{A}_{mAP} \uparrow$   | 0.80  | 2.89  | 2.92  | 2.48  |
| $\mathcal{A}_{NDS} \uparrow$   | 2.05  | 2.54  | 2.28  | 2.10  |
| $\mathcal{A}_{ATE} \downarrow$ | -2.16 | -1.92 | -2.00 | -1.41 |
| $\mathcal{A}_{ASE} \downarrow$ | -2.43 | -1.21 | -1.22 | -1.01 |
| $\mathcal{A}_{AOE} \downarrow$ | -3.06 | -1.59 | -0.74 | -2.02 |
| $\mathcal{A}_{AVE} \downarrow$ | -5.51 | -4.19 | -2.43 | -2.22 |
| $\mathcal{A}_{AAE} \downarrow$ | -3.75 | -2.08 | -1.78 | -1.93 |

Intuitively, increasing the number of GMM components  $K$  allows the RoI detector to better fit the object point clouds (the learning objective will be the same as point cloud segmentation when  $K \rightarrow \infty$ ), so RoIs will contain fewer background points. However, as shown in Ta-

ble 4, the performance of DetVPCC starts to decline when  $K = 7$ . This can be attributed to the observation that a simpler object representation tends to stabilize the learning process [51, 55]. Additionally, the benefits of a more precise fit diminish when  $K$  becomes large, as the number of background points involved in heatmaps is already minimized.

#### 4.3.3 Heatmap Binarization Threshold

Table 5. Impact of heatmap binarization threshold

| $\gamma$                       | 0.2   | 0.3   | 0.4   | 0.5   |
|--------------------------------|-------|-------|-------|-------|
| $\mathcal{A}_{mAP} \uparrow$   | -0.69 | 1.67  | 2.92  | 2.80  |
| $\mathcal{A}_{NDS} \uparrow$   | -1.06 | 1.37  | 2.28  | 2.64  |
| $\mathcal{A}_{ATE} \downarrow$ | 0.96  | -1.19 | -2.00 | -2.10 |
| $\mathcal{A}_{ASE} \downarrow$ | 0.00  | -0.82 | -1.22 | -1.54 |
| $\mathcal{A}_{AOE} \downarrow$ | 2.49  | -0.68 | -0.74 | -2.31 |
| $\mathcal{A}_{AVE} \downarrow$ | 4.04  | -1.50 | -2.43 | -4.29 |
| $\mathcal{A}_{AAE} \downarrow$ | -0.38 | -1.17 | -1.78 | -2.20 |

Table 5 shows the impact of the heatmap binarization threshold  $\gamma$ . It can be seen that  $\gamma = 0.4$  achieves the best mAP and NDS performance. When  $\gamma$  is too small, the predicted RoI regions will include too many non-RoI points, leading to poor compression efficiency. On the contrary, when  $\gamma$  is too large, potential objects may be ignored, leading to low detection accuracy. It is worth noting that  $\gamma = 0.5$  shows improvement on true-positive metrics. It is expected because regions with higher heatmap scores are inherently easier to identify and localize.

#### 4.3.4 Ablation on Ground Removal

Table 6. Ablation on ground removal

| Ground Removal                 | w/    | w/o   |
|--------------------------------|-------|-------|
| $\mathcal{A}_{mAP} \uparrow$   | 2.92  | 1.82  |
| $\mathcal{A}_{NDS} \uparrow$   | 2.28  | 1.15  |
| $\mathcal{A}_{ATE} \downarrow$ | -2.00 | -0.55 |
| $\mathcal{A}_{ASE} \downarrow$ | -1.22 | -0.76 |
| $\mathcal{A}_{AOE} \downarrow$ | -0.74 | -0.74 |
| $\mathcal{A}_{AVE} \downarrow$ | -2.43 | 0.62  |
| $\mathcal{A}_{AAE} \downarrow$ | -1.78 | -0.96 |

Table 6 shows the contribution of ground removal in DetVPCC. Ground removal assists the performance of DetVPCC to some extent as it compensates for the 2D heatmap on the z-axis and helps filter the ground points.

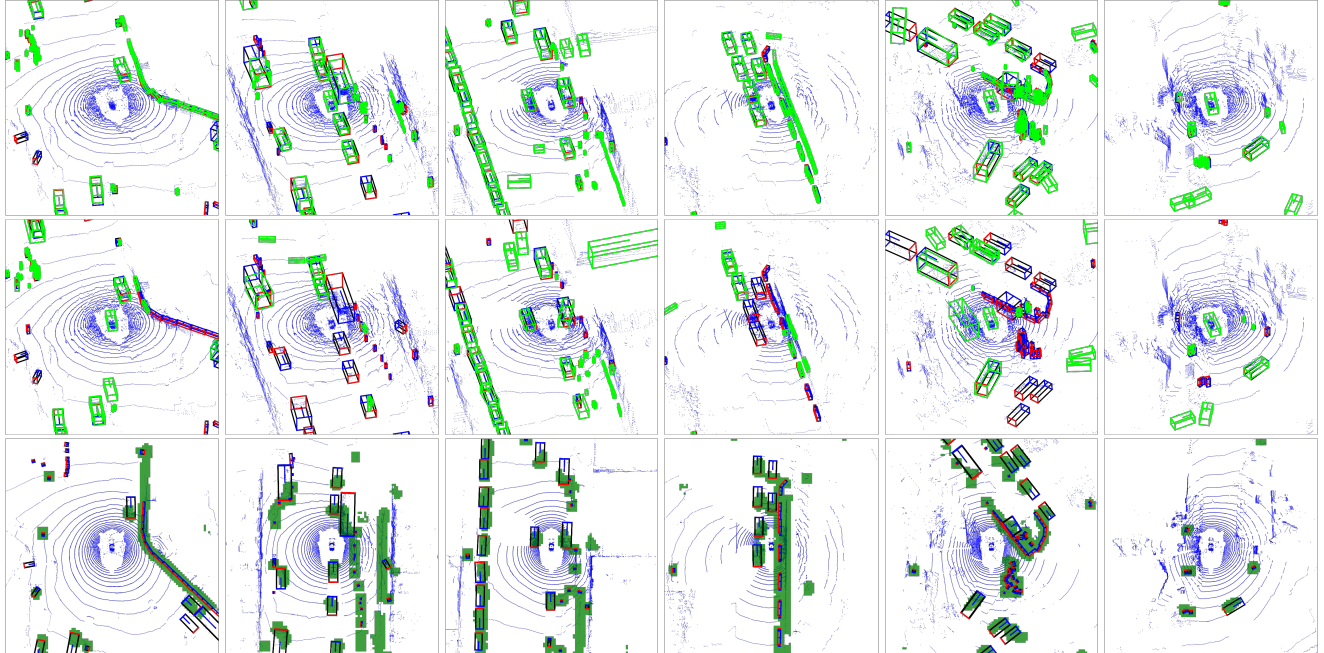


Figure 6. Qualitative results. The first and second rows are the detection results of CenterPoint on point clouds encoded with DetVPCC and VPCC, respectively, where  $q_r = 20$  and  $q_b = 45$ . The third row shows RoIs (colored in green) predicted by the ROI detector.

However, DetVPCC still outperforms vanilla VPCC without ground removal, proving its effectiveness. In contrast, the naive ROI detector, which is also equipped with ground removal, exhibits compromised performance as mentioned in Sec. 4.2.

#### 4.3.5 Find Points in Bounding Boxes

Table 7. Speed test of Alg. 1

| Method            | Ours | nuScenes Toolkit |
|-------------------|------|------------------|
| Time per Box (ms) | 0.70 | 2.15             |

Table. 7 evaluates the speed of Alg. 1. The baseline method is the *points\_in\_box* function provided by nuScenes toolkit<sup>5</sup>, which examines each point’s relative position to the bounding box’s three axes. Experiments are conducted on Intel Xeon Gold 6226R CPUs. As shown, our method is  $\sim 3\times$  faster than the baseline method. The speed-up is attributed to the reusable K-D tree that drastically narrows the search space and cuts unnecessary evaluation between points and boxes that are too far away.

#### 4.4. Qualitative Results

Fig. 6 shows visualized detection results between DetVPCC and vanilla VPCC, along with heatmaps predicted by the ROI detector. It can be seen that ROI-based encoding significantly aids 3D object detection, especially for small objects that are easily lost by vanilla VPCC.

<sup>5</sup><https://github.com/nuTonomy/nuScenes-devkit>

## 5. Limitations and Future Works

While this work primarily focuses on developing an ROI-based point cloud sequence encoder for 3D object detectors, as well as an efficient ROI detector, several aspects remain for future exploration: 1) For simplicity, pre-trained backend 3D object detectors are fine-tuned on uniformly compressed point clouds. The unseen ROI-encoded point cloud may compromise detection accuracy. 2) We use a constant ROI QP for all point cloud frames in a sequence. Dynamic ROI QP assignment according to the frame’s complexity may further improve the compression efficiency. 3) We assume RoIs are exactly where objects are located. However, non-object regions may also contain information critical for object identification. A more adaptive ROI design may further improve the performance. 4) Our method could be extended from autonomous driving scenes to support a broader range of applications, such as indoor 3D scene understanding [3, 12].

## 6. Conclusion

In this paper, we introduce DetVPCC, a ROI-based point cloud sequence compression framework. We implemented and evaluated DetVPCC on the nuScenes dataset, and the results show its superiority. We believe the proposed method can potentially alleviate the storage and network bandwidth demands of point cloud-based object detection systems through its efficient ROI-based encoding scheme.

## References

- [1] nuscenescenes.org. <https://www.nuscenes.org/object-detection>. [Accessed 29-10-2024]. 5
- [2] Anique Akhtar, Zhu Li, and Geert Van der Auwera. Inter-frame compression for dynamic point cloud geometry coding. *IEEE Transactions on Image Processing*, 2024. 2
- [3] Iro Armeni, Ozan Sener, Amir R. Zamir, Helen Jiang, Ioannis Brilakis, Martin Fischer, and Silvio Savarese. 3d semantic parsing of large-scale indoor spaces. In *Proceedings of the IEEE International Conference on Computer Vision and Pattern Recognition*, 2016. 8
- [4] C Bradford Barber, David P Dobkin, and Hannu Huhdanpaa. The quickhull algorithm for convex hulls. *ACM Transactions on Mathematical Software (TOMS)*, 22(4):469–483, 1996. 5
- [5] Csaba Benedek. 3D people surveillance on range data sequences of a rotating Lidar. *Pattern Recognition Letters*, 50: 149–158, 2014. 1
- [6] Miquel Romero Blanch, Zenjie Li, Sergio Escalera, and Kamal Nasrollahi. Lidar-assisted 3d human detection for video surveillance. In *Proceedings of the IEEE/CVF Winter Conference on Applications of Computer Vision*, pages 123–131, 2024. 1
- [7] Holger Caesar, Varun Bankiti, Alex H. Lang, Sourabh Vora, Venice Erin Liong, Qiang Xu, Anush Krishnan, Yu Pan, Giancarlo Baldan, and Oscar Beijbom. nuScenes: A Multimodal Dataset for Autonomous Driving. In *2020 IEEE/CVF Conference on Computer Vision and Pattern Recognition (CVPR)*, pages 11618–11628, Seattle, WA, USA, 2020. IEEE. 1, 2, 5, 6
- [8] MMDetection3D Contributors. MMDetection3D: OpenMMLab next-generation platform for general 3D object detection. <https://github.com/open-mmlab/mmdetection3d>, 2020. 5, 1
- [9] Ricardo L De Queiroz and Philip A Chou. Motion-compensated compression of dynamic voxelized point clouds. *IEEE Transactions on Image Processing*, 26(8): 3886–3895, 2017. 2
- [10] Kuntai Du, Ahsan Pervaiz, Xin Yuan, Aakanksha Chowdhery, Qizheng Zhang, Henry Hoffmann, and Junchen Jiang. Server-driven video streaming for deep learning inference. In *Proceedings of the Annual conference of the ACM Special Interest Group on Data Communication on the applications, technologies, architectures, and protocols for computer communication*, pages 557–570, 2020. 2
- [11] Kuntai Du, Qizheng Zhang, Anton Arapin, Haodong Wang, Zhengxu Xia, and Junchen Jiang. Accmpeg: Optimizing video encoding for video analytics. *arXiv preprint arXiv:2204.12534*, 2022. 2
- [12] Dai et al. Scannet: Richly-annotated 3d reconstructions of indoor scenes. In *CVPR, IEEE*, 2017. 8
- [13] Duarte Fernandes, António Silva, Rafael Névoa, Cláudia Simões, Dibet Gonzalez, Miguel Guevara, Paulo Novais, João Monteiro, and Pedro Melo-Pinto. Point-cloud based 3D object detection and classification methods for self-driving applications: A survey and taxonomy. *Information Fusion*, 68:161–191, 2021. 1
- [14] Diogo C Garcia, Tiago A Fonseca, Renan U Ferreira, and Ricardo L De Queiroz. Geometry coding for dynamic voxelized point clouds using octrees and multiple contexts. *IEEE Transactions on Image Processing*, 29:313–322, 2019. 2
- [15] Pedro Gomes. Graph-based network for dynamic point cloud prediction. In *Proceedings of the 12th ACM Multimedia Systems Conference*, pages 393–397, 2021. 2
- [16] D. Graziosi, O. Nakagami, S. Kuma, A. Zaghetto, T. Suzuki, and A. Tabatabai. An overview of ongoing point cloud compression standardization activities: video-based (V-PCC) and geometry-based (G-PCC). *APSIPA Transactions on Signal and Information Processing*, 9(1), 2020. 1, 2, 3
- [17] Danillo Bracco Graziosi. Video-based dynamic mesh coding. In *2021 IEEE International Conference on Image Processing (ICIP)*, pages 3133–3137. IEEE, 2021. 1
- [18] Hexagon. Discover 3d surveillance, 2021. 1
- [19] M. Himmelsbach, Felix v. Hundelshausen, and H.-J. Wuen-sche. Fast segmentation of 3D point clouds for ground vehicles. In *2010 IEEE Intelligent Vehicles Symposium*, pages 560–565, 2010. ISSN: 1931-0587. 1
- [20] Diederik P Kingma. Adam: A method for stochastic optimization. *arXiv preprint arXiv:1412.6980*, 2014. 1
- [21] Alex H Lang, Sourabh Vora, Holger Caesar, Lubing Zhou, Jiong Yang, and Oscar Beijbom. Pointpillars: Fast encoders for object detection from point clouds. In *Proceedings of the IEEE/CVF conference on computer vision and pattern recognition*, pages 12697–12705, 2019. 5
- [22] Hei Law and Jia Deng. Cornernet: Detecting objects as paired keypoints. In *Proceedings of the European conference on computer vision (ECCV)*, pages 734–750, 2018. 4, 5
- [23] Seungjae Lee, Hyungtae Lim, and Hyun Myung. Patchwork++: Fast and robust ground segmentation solving partial under-segmentation using 3D point cloud. In *Proc. IEEE/RSJ Int. Conf. Intell. Robots Syst.*, pages 13276–13283, 2022. 5
- [24] Seungjae Lee, Hyungtae Lim, and Hyun Myung. Patchwork++: Fast and Robust Ground Segmentation Solving Partial Under-Segmentation Using 3D Point Cloud. In *2022 IEEE/RSJ International Conference on Intelligent Robots and Systems (IROS)*, pages 13276–13283, 2022. ISSN: 2153-0866. 1
- [25] Xin Li, Jun Shi, and Zhibo Chen. Task-driven semantic coding via reinforcement learning. *IEEE Transactions on Image Processing*, 30:6307–6320, 2021. 2
- [26] Alexander Lianides, Isaac Chan, Mohamed Ismail, Ian Harshbarger, Marco Levorato, Davide Callegaro, and Sharon LG Contreras. 3d object detection for aerial platforms via edge computing: An experimental evaluation. In *2022 18th International Conference on Distributed Computing in Sensor Systems (DCOSS)*, pages 252–260. IEEE, 2022. 1
- [27] Lei Liu, Zhihao Hu, and Jing Zhang. Pchm-net: A new point cloud compression framework for both human vision and machine vision. In *2023 IEEE International Conference on Multimedia and Expo (ICME)*, pages 1997–2002. IEEE, 2023. 2

- [28] Shengzhong Liu, Tianshi Wang, Jinyang Li, Dachun Sun, Mani Srivastava, and Tarek Abdelzaher. Adamask: Enabling machine-centric video streaming with adaptive frame masking for dnn inference offloading. In *Proceedings of the 30th ACM international conference on multimedia*, pages 3035–3044, 2022. 2
- [29] Zhijian Liu, Haotian Tang, Alexander Amini, Xinyu Yang, Huizi Mao, Daniela L Rus, and Song Han. Bevfusion: Multi-task multi-sensor fusion with unified bird’s-eye view representation. In *2023 IEEE international conference on robotics and automation (ICRA)*, pages 2774–2781. IEEE, 2023. 1, 5
- [30] Jiageng Mao, Shaoshuai Shi, Xiaogang Wang, and Hongsheng Li. 3D Object Detection for Autonomous Driving: A Comprehensive Survey. *International Journal of Computer Vision*, 131(8):1909–1963, 2023. 1
- [31] Fraser McLean, Leyang Xue, Chris Xiaoxuan Lu, and Mahesh Marina. Towards edge-assisted real-time 3d segmentation of large scale lidar point clouds. In *Proceedings of the 6th International Workshop on Embedded and Mobile Deep Learning*, pages 1–6, 2022. 1
- [32] Rufael Mekuria, Sebastien Laserre, and Christian Tulvan. Performance assessment of point cloud compression. In *2017 IEEE Visual Communications and Image Processing (VCIP)*, pages 1–4, 2017. 1
- [33] Taslim Murad, Anh Nguyen, and Zhisheng Yan. Dao: Dynamic adaptive offloading for video analytics. In *Proceedings of the 30th ACM International Conference on Multimedia*, pages 3017–3025, 2022. 2
- [34] Nvidia. NVENC Video Encoder API - Emphasis MAP, 2021. 3
- [35] Anshul Paigwar, David Sierra-Gonzalez, Özgür Ercent, and Christian Laugier. Frustum-pointpillars: A multi-stage approach for 3d object detection using rgb camera and lidar. In *Proceedings of the IEEE/CVF international conference on computer vision*, pages 2926–2933, 2021. 1
- [36] Charles R Qi, Wei Liu, Chenxia Wu, Hao Su, and Leonidas J Guibas. Frustum pointnets for 3d object detection from rgb-d data. In *Proceedings of the IEEE conference on computer vision and pattern recognition*, pages 918–927, 2018. 1
- [37] Christoph Reich, Biplob Debnath, Deep Patel, Tim Prange-meier, Daniel Cremers, and Srimat Chakradhar. Deep video codec control for vision models. In *Proceedings of the IEEE/CVF Conference on Computer Vision and Pattern Recognition*, pages 5732–5741, 2024. 2
- [38] Iain E. Garden Richardson. H. 264/mpeg-4 part 10 white peper : Transform & quantization. 2003. 3
- [39] Michael Rudolph, Stefan Schneegass, and Amr Rizk. Rabbit: Live transcoding of v-pcc point cloud streams. In *Proceedings of the 14th Conference on ACM Multimedia Systems*, pages 97–107, 2023. 3
- [40] Khadija Shaheen, Muhammad Abdullah Hanif, Osman Hasan, and Muhammad Shafique. Continual learning for real-world autonomous systems: Algorithms, challenges and frameworks. *Journal of Intelligent & Robotic Systems*, 105(1):9, 2022. 1
- [41] Fangyu Shen and Wei Gao. A rate control algorithm for video-based point cloud compression. In *2021 International Conference on Visual Communications and Image Processing (VCIP)*, pages 1–5. IEEE, 2021. 3
- [42] Xuebin Sun, Sukai Wang, Miaohui Wang, Shing Shin Cheng, and Ming Liu. An advanced lidar point cloud sequence coding scheme for autonomous driving. In *Proceedings of the 28th ACM International Conference on Multimedia*, pages 2793–2801, 2020. 2
- [43] Dong Tian, Hideaki Ochimizu, Chen Feng, Robert Cohen, and Anthony Vetro. Geometric distortion metrics for point cloud compression. In *2017 IEEE International Conference on Image Processing (ICIP)*, pages 3460–3464, 2017. ISSN: 2381-8549. 1
- [44] Shuoqian Wang, Mufeng Zhu, Na Li, Mengbai Xiao, and Yao Liu. Vqba: Visual-quality-driven bit allocation for low-latency point cloud streaming. In *Proceedings of the 31st ACM International Conference on Multimedia*, pages 9143–9151, 2023. 3
- [45] Yiding Wang, Weiyang Wang, Duowen Liu, Xin Jin, Junchen Jiang, and Kai Chen. Enabling edge-cloud video analytics for robotics applications. *IEEE Transactions on Cloud Computing*, 11(2):1500–1513, 2022. 2
- [46] Thomas Wiegand, Gary J Sullivan, Gisle Bjontegaard, and Ajay Luthra. Overview of the h. 264/avc video coding standard. *IEEE Transactions on circuits and systems for video technology*, 13(7):560–576, 2003. 1, 3
- [47] Cristian Wisultschew, Gabriel Mujica, Jose Manuel Lanza-Gutierrez, and Jorge Portilla. 3D-LIDAR Based Object Detection and Tracking on the Edge of IoT for Railway Level Crossing. *IEEE Access*, 9:35718–35729, 2021. Conference Name: IEEE Access. 1
- [48] Xuedou Xiao, Juecheng Zhang, Wei Wang, Jianhua He, and Qian Zhang. Dnn-driven compressive offloading for edge-assisted semantic video segmentation. In *IEEE INFOCOM 2022-IEEE Conference on Computer Communications*, pages 1888–1897. IEEE, 2022. 2
- [49] Xiufeng Xie and Kyu-Han Kim. Source compression with bounded dnn perception loss for iot edge computer vision. In *The 25th Annual International Conference on Mobile Computing and Networking*, pages 1–16, 2019. 2
- [50] Rui Yang. *Online continual learning for 3D detection of road participants in autonomous driving*. PhD thesis, Université Bourgogne Franche-Comté, 2023. 1
- [51] Tianwei Yin, Xingyi Zhou, and Philipp Krahenbuhl. Center-based 3d object detection and tracking. In *Proceedings of the IEEE/CVF conference on computer vision and pattern recognition*, pages 11784–11793, 2021. 1, 4, 5, 7
- [52] Yiming Zeng, Yu Hu, Shice Liu, Jing Ye, Yinhe Han, Xi-aowei Li, and Ninghui Sun. RT3D: Real-Time 3-D Vehicle Detection in LiDAR Point Cloud for Autonomous Driving. *IEEE Robotics and Automation Letters*, 3(4):3434–3440, 2018. Conference Name: IEEE Robotics and Automation Letters. 1
- [53] Miao Zhang, Fangxin Wang, and Jiangchuan Liu. Casva: Configuration-adaptive streaming for live video analytics. In *IEEE INFOCOM 2022-IEEE Conference on Computer Communications*, pages 2168–2177. IEEE, 2022. 2
- [54] Tianchen Zhao, Xuefei Ning, Ke Hong, Zhongyuan Qiu, Pu Lu, Yali Zhao, Linfeng Zhang, Lipu Zhou, Guohao Dai,

Huazhong Yang, et al. Ada3d: Exploiting the spatial redundancy with adaptive inference for efficient 3d object detection. In *Proceedings of the IEEE/CVF International Conference on Computer Vision*, pages 17728–17738, 2023. [4](#)

- [55] Xingyi Zhou, Dequan Wang, and Philipp Krähenbühl. Objects as points. *arXiv preprint arXiv:1904.07850*, 2019. [4](#),

# DetVPCC: RoI-based Point Cloud Sequence Compression for 3D Object Detection

## Supplementary Material

### 7. Details of RoI detectors

#### 7.1. Header Design

Inspired by CenterPoint [51], we separate the heatmap predictions of objects with different sizes into 6 tasks. Backbone features first pass through a shared convolution block, which includes a  $3 \times 3$  convolution layer, a batch normalization layer, and a ReLU activation layer. The output of the first convolution block is then fed into separate task-specific branches for each task. Each task branch contains a deformable convolution layer with a group size of 4, a convolution block with a  $3 \times 3$  convolution layer, a batch normalization layer, and a ReLU layer, followed by a  $3 \times 3$  convolution output layer.

#### 7.2. Training

We implement our RoI detector in PyTorch using the open-sourced MMDetection3D [8]. We train the model for 20 epochs for the RoI detector using the Adam [20] optimizer with a learning rate of  $10^{-4}$ , batch size of 9, and a weight decay of 0.01.

### 8. Details of Back-end 3D Object Detectors

#### 8.1. Training

We pre-train the back-end detectors with lossless point clouds following the settings in MMDetection3D [8]. Specifically, we train each detector for 20 epochs using the Adam optimizer. The batch size is set to 9, the learning rate is set to  $10^{-4}$ , and the weight decay is set to 0.01. We then fine-tune detectors on a mixed dataset for one epoch using the same training parameters in the pre-training phase. The mixed dataset is a uniform mixture of training sets encoded by vanilla VPCC with  $QP \in \{20, 25, 30\}$  and lossless encoding.

#### 8.2. Complexity

Table 8 shows the complexities of the back-end detectors.

Table 8. Complexities of back-end detectors.

| Model | CenterPoint |           | BEVFusion-Lidar |           |
|-------|-------------|-----------|-----------------|-----------|
|       | FLOPs (G)   | Param (M) | FLOPs (G)       | Param (M) |
| Total | 119.33      | 6.11      | 85.98           | 5.15      |

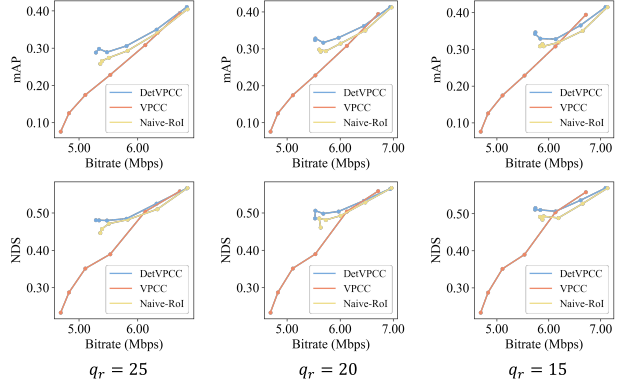


Figure 7. Metric-bitrate curve in Sec. 4.2 (CenterPoint)

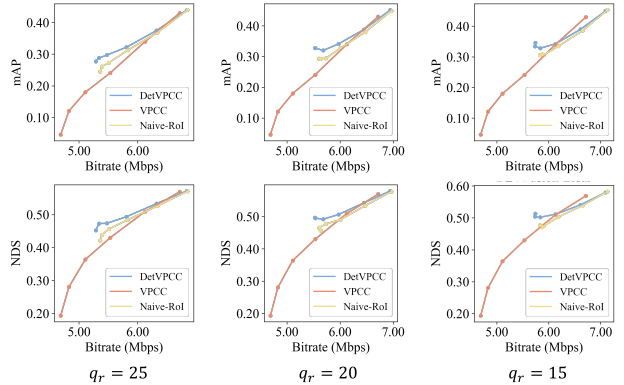


Figure 8. Metric-bitrate curve in Sec. 4.2 (BEVFusion-Lidar)

### 9. Metric-bitrate Curves in Main Results

Fig. 7 and Fig. 8 give the mAP-bitrate and NDS-bitrate curves of DetVPCC, VPCC and Naive RoI in Sec. 4.2.